Numerical Simulation of Tip Vortices of Wings in Subsonic and Transonic Flows

G. R. Srinivasan*
JAI Associates, Inc., Mountain View, California
and
W. J. McCroskey,† J. D. Baeder,‡ and T. A. Edwards§
NASA Ames Research Center, Moffett Field, California

A multiblock zonal algorithm is used to solve numerically the thin-layer Navier-Stokes and the Euler equations for simulating the flowfields of isolated wings, with particular emphasis on understanding the formation and roll-up of tip vortices in subsonic and transonic flows. Four test cases consisting of wings of different planforms have been considered to examine the influence of the tip-cap shape, tip planform, and freestream Mach number. Comparison of the numerical results with the available experimental data shows good agreement for the surface pressures in the regions where the flow is attached or mildly separated. However, discrepancies exist in regions of massive shock-induced separation in transonic flow and in the immediate vicinity of the wing tip in subsonic flow. In general, a fairly good definition of the formation and roll-up of the tip vortex is demonstrated for all of the cases considered here, subject to the coarseness of the grid in the far field. Finally, the calculated lift, drag, and pitching-moment coefficients agree well with the experimentally determined values, where available.

Nomenclature

B = semispan of the wing
C = root chord of the wing
C_D, C_L = drag and lift coefficients, respectively
C_M = quarter-chord pitching-moment coefficient
C_p = pressure coefficient
$\hat{E}, \hat{F}, \hat{G}$ = flux vectors
M_∞ = freestream Mach number
$\hat{Q}$ = flowfield vector
q = velocity vector
Re = Reynolds number
$\hat{S}$ = viscous flux vector
u_∞ = freestream velocity
x, y, z, t = physical space coordinates
α = angle of attack, deg
Γ_V = dimensionless strength of tip vortex, normalized by u_∞ and C
ξ, η, ζ, τ = generalized curvilinear coordinates

Introduction

THE process of formation of a tip vortex and its subsequent roll-up in the downstream wake of a wing or helicopter blade constitute a problem of fundamental importance in fluid mechanics, but one with important practical applications. The tip vortex evolves from a complex three-dimensional separated flow that is difficult to analyze. Despite a large number of theoretical and experimental studies, the present understanding of such flows remains essentially qualitative, especially regarding the detailed mechanics of vorticity transport from the viscous layers near the surface into the trailing concentrated vortex.

The hazards of concentrated vortices in the wakes of large aircraft are well known. Rotating blades, such as propellers and helicopter rotors, also generate complex vortical wakes that interact with the following blades. Such an interaction is responsible for unsteady aerodynamic loads, which in turn affect performance, vibration, and aeroacoustic characteristics. A detailed study of the formation and initial roll-up of such concentrated vortices and the dependence of these processes on the geometry of the blades is an important step toward altering the structure of these vortices and minimizing their adverse influence.

The recent numerical simulation of the viscous flow in the tip region of a transonic swept wing by Mansour[1] is a pioneering work, and Kaynak et al.[2] have extended this research to explore the details of three-dimensional shock-induced separation using a multiblock Euler/Navier-Stokes zonal method. The present study further extends the numerical simulation of this class of problems at both subsonic and transonic conditions, using this multiblock zonal method. Particular emphasis is placed on the flowfield in the tip region and the vortex-formation process. The surface and flowfield topologies are presented for four different wing shapes, and the influence of the tip geometry and wing planform is discussed. The numerical results are compared with the available experimental data.

Governing Equations and Numerical Scheme

The governing partial differential equations are the thin-layer Navier-Stokes and the Euler equations. The equations are transformed to the arbitrary curvilinear space (ξ, η, ζ, τ)

Presented as Paper 86-1095 at the AIAA/ASME 4th Fluid Mechanics, Plasma Dynamics, and Lasers Conference, Atlanta, GA, May 12-14, 1986; received March 9, 1987; revision received Nov. 12, 1987. This paper is declared a work of the U.S. Government and therefore is in the public domain.

*Senior Research Scientist. Associate Fellow AIAA.
†Senior Staff Scientist, U.S. Army Aeroflightdynamics Directorate —AVSCOM. Associate Fellow AIAA.
†Research Scientist, U.S. Army Aeroflightdynamics Directorate —AVSCOM. Member AIAA.
§Research Scientist. Member AIAA.

while retaining strong conservation law form to capture shock waves. The transformed equations written in generalized curvilinear coordinates are given by[3,4]

$$\partial_\tau \hat{Q} + \partial_\xi \hat{E} + \partial_\eta \hat{F} + \partial_\zeta \hat{G} = \epsilon Re^{-1} \partial_\zeta \hat{S} \tag{1}$$

where

$$\hat{Q} = J^{-1} \begin{bmatrix} \rho \\ \rho u \\ \rho v \\ \rho w \\ e \end{bmatrix}, \quad \hat{E} = J^{-1} \begin{bmatrix} \rho U \\ \rho u U + \xi_x p \\ \rho v U + \xi_y p \\ \rho w U + \xi_z p \\ U(e+p) - \xi_t p \end{bmatrix}$$

$$\hat{F} = J^{-1} \begin{bmatrix} \rho V \\ \rho u V + \eta_x p \\ \rho v V + \eta_y p \\ \rho w V + \eta_z p \\ V(e+p) - \eta_t p \end{bmatrix}, \quad \hat{G} = J^{-1} \begin{bmatrix} \rho W \\ \rho u W + \zeta_x p \\ \rho v W + \zeta_y p \\ \rho w W + \zeta_z p \\ W(e+p) - \zeta_t p \end{bmatrix} \tag{2}$$

and $\epsilon = 0$ for Euler equations, and $\epsilon = 1$ for thin-layer Navier-Stokes equations. The primitive variables of Eq. (1), namely, ρ, ρu, ρv, ρw, and e, are normalized by the freestream reference quantities. The characteristic length and velocity scales are given by the wing root chord and the freestream sound speed, respectively. The viscous flux vector $\hat{S}$ used here is in the limit of thin-layer approximation, the relations for the contravariant velocities U, V, and W, the metrics ξ_x, ξ_y, ξ_z, etc., and the Jacobian of transformation J are described in detail in Refs. 4 and 5.

The velocity components u, v, w and the pressure p are related to the total energy per unit volume e through the equation of state for a perfect gas by

$$p = (\gamma - 1)\,[e = (\rho/2)\,(u^2 + v^2 + w^2)] \tag{3}$$

The numerical code that solves these equations, called ARC3D,[4] was adapted by Holst et al.[5] and Flores[6] to develop the transonic Navier-Stokes (TNS) multiblock zonal algorithm. This code retains all of the important features of the ARC3D code and, in addition, has the advantage of dealing with multiple blocks. The details of the development of this four block version of the TNS wing code and improvements to enhance its efficiency for multiple zones are described in the papers of Holst et al.[5] and Flores.[6] In addition to the example solutions for isolated wings discussed in these two papers, Kaynak et al.[2] have reported further refinements to this code to analyze the flow topology of shock-induced separated flows on wings in transonic flows. The current version of this four block scheme is used mainly for computing the flowfields of isolated wings, with or without wind-tunnel walls.

The five important features of the TNS code are:

1) The thin-layer Navier-Stokes equations and the Euler equations are solved in strong conservation law form to capture shock waves.

2) The convergence procedure is significantly accelerated over the standard ARC3D code for one block[4] because the present scheme solves the Euler equations over a significant part of the flow domain.

3) Two numerical options are available for solving the equations. One is based on the standard ADI algorithm of Beam and Warming,[7] which solves the block-tridiagonal matrices along each coordinate direction. The other is based on the diagonalized algorithm of Pulliam and Chaussee,[8] which solves a set of five scalar pentadiagonal matrices along each coordinate direction.

4) The diagonal algorithm has been implemented with two options of variable time-step philosophies to accelerate the convergence rate of the numerical scheme, that is, one that scales the marching time-step with the local Jacobian, as suggested by Srinivasan et al.,[9] and the other that scales the time step using a combination of the Jacobian and local solution variation.[4,6]

5) The code is vectorized for the Cray-XMP and Cray-2 supercomputers.

Both the numerical codes (TNS and ARC3D) use the standard second-order-accurate central differencing to construct the appropriate spatial differencing scheme. The diagonal version, which is used in the present study to calculate steady-state solutions, uses fourth-order-accurate smoothing operators on the implicit and explicit sides of the numerical algorithm for controlling nonlinear stability of the numerical scheme. In the present calculations, a turbulent boundary layer is assumed for the entire wing, and the Baldwin and Lomax algebraic turbulence model[10] is used to calculate the turbulent eddy viscosity. Although this model has some limitations, it has been effectively applied to a variety of two- and three-dimensional flow problems involving mild separation.

Grid Generation and Data Management

The details of the grid-generation scheme and the data management system are described in Ref. 5. For the sake of completeness, the important steps necessary to generate a working finite-difference grid are described here. First, a coarse grid encompassing the entire flowfield is generated using the parabolic grid-generation scheme of Edwards.[11] This single-block grid has an H-grid topology in both the spanwise and chordwise directions. The grid is further subdivided into four zones by means of the zoning algorithm in the TNS code. Thus the complete flow domain is divided into four blocks. Figure 1 is a pictorial view of one such grid topology for a low-aspect-ratio wing. In this view, for clarity, only the grid at the symmetry plane of the wing is shown. The coarse outer (inviscid) grid, marked as block 1, is shown in white; the finer inviscid grid, marked as block 2, is shown in red. The two yellow blocks adjacent to the wing and on either side of it, marked as blocks 3 and 4, are the viscous zones that have fine clustering in the normal direction to resolve the boundary layer, in the streamwise direction at the leading-edge and trailing-edge regions, and in the spanwise direction at the wing-tip region to

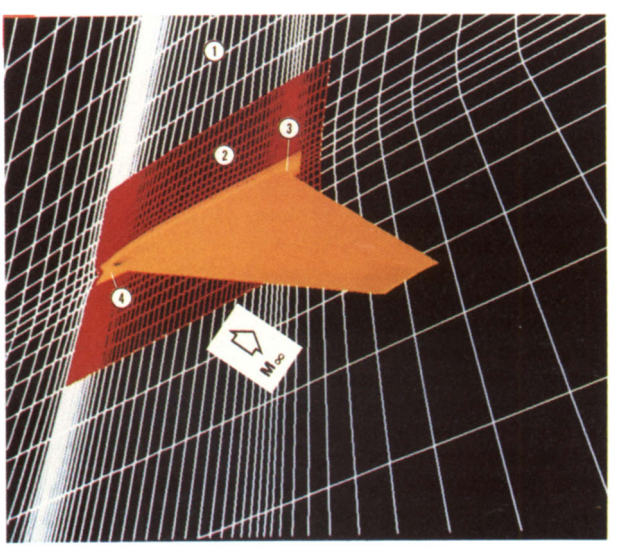

Fig. 1 Typical zonal grid topology. Outer zones identified as 1 and 2 are inviscid zones; inner zones 3 and 4 are viscous zones.

resolve the tip vortex. The inviscid grids also have appropriate clustering likewise.

Most of the calculations were done with a default grid consisting typically of over 40,000 grid points in each of the four zones. For such a grid, the wing tip was assumed to have a beveled (or a triangular) tip cap. Although the grid geometry for each wing discussed here depended on the aspect ratio of the individual wing geometry, the spanwise grid spacing in the wing-tip region and the spacing in the normal direction to the wing surface were kept the same for all the wings, that is, 0.015 and 0.15 C in the coarse grid. The viscous blocks (of size 0.15 C) had 25 finely clustered grid points in the normal direction for all the wings with the spacing at the surface equal to 1×10^{-5} C.

To examine the effect of the tip-cap shape, a squared (flat) tip and a rounded (body of revolution) tip were also considered for the rectangular wing in subsonic flow. In order to get a good definition of these tip profiles, the spanwise clustering had to be increased near the tip region. These grids had nearly 90,000 grid points in each zone. The spacing of the grid at the wall in the normal direction was the same as specified earlier but, at the tip cap, it was reduced to 0.004 in the spanwise direction.

The data management strategy has been discussed by Holst et al.[5] and also by Kaynak et al.[2] In brief, the base grid, which is usually generated outside the TNS code, is read in first, and this grid is further divided into appropriate zones by the "zoner" code. Once this is done, the flow solver is initiated. The iteration procedure starts in the outer inviscid zone or block and proceeds into the inner viscous blocks. The information necessary to update the boundary conditions at the zonal interface is found from the neighboring zones through a series of one-dimensional linear interpolations. Such a scheme lends itself to a conservative treatment of the boundaries and thus captures distortion-free movement of discontinuities across the boundaries.

In the solution procedure, only the information necessary to solve each zone resides at any one time in the main memory of the Cray-XMP computer. The information on zones that are not being computed is temporarily stored on the solid state device (SSD). The use of SSD frees the main memory of the space otherwise taken by the data stored on the SSD and enables use of (allowable) maximum number of grid points for the flowfield. Also, use of SSD reduces the I/O wait time significantly.[6]

Boundary Conditions

Since the TNS code is a multiblock zonal algorithm, there are two types of boundaries where conditions have to be specified: 1) the physical boundaries, such as inflow, outflow, and solid surfaces, and 2) the zonal boundaries across which all flow quantities must be continuous. All of the boundary and zonal interface conditions are applied explicitly.

At the far-field boundaries, which are typically 6–10 chords away from the wing, freestream values are specified for all the flow quantities. At the outflow boundaries, zeroth-order extrapolation is used from the grid interior. At the symmetry plane, a zeroth-order extrapolation is used for the density and a first-order extrapolation for the x component and the z component of velocities while the spanwise velocity component is set to zero to force symmetry. A first-order extrapolation is also used for the pressure, and the energy is calculated from the equation of state. At the surface of the wing, a no-slip condition is used for the velocity components, and the pressure is calculated by solving the normal momentum equation at the surface. In the spirit of thin-layer approximation, the normal momentum equation reduces to $dp/dn=0$, where n is the local normal to the surface. Density is determined by assuming an adiabatic wall condition. Given the pressure p and the density ρ at the wall, the total energy e is determined from Eq. (3). The details of the zonal interface boundary conditions are described in Refs. 2 and 5.

Results and Discussion

In this section, numerical results are presented at subsonic and transonic flow conditions for four isolated wing configurations. These results are compared with the available experimental data. The different flow conditions and the wing geometries considered consist of: 1) a rectangular wing with an aspect ratio (based on semispan) of 2.5 without twist or taper, in a uniform flow of $M_\infty=0.17$ at $\alpha=5$ deg and $Re=2\times10^6$; 2) a typical fighter aircraft wing with twist and taper and an aspect ratio of 0.83 in a uniform flow of $M_\infty=0.9$ at $\alpha=5$ deg and $Re=6.8\times10^6$; and 3) two wings with exotic tip shapes typifying helicopter rotor blades, with aspect ratios of 5.0 at $M_\infty=0.85$, $\alpha=5$ deg, and $Re=8.5\times10^6$. The planforms and surface grids of these wing geometries are shown in Fig. 2.

Rectangular Wing in Subsonic Flow

The rectangular wing configuration and the subsonic flow conditions considered here correspond to the experimental test case of Spivey and Moorhouse,[12,13] with the test conditions just described. The wing section is made up of an NACA-0015 airfoil and has no twist or taper. Although Spivey and Moorhouse, in their experiments, chose a wing with only a square (or flat) tip configuration, the present calculations consider three different tip-cap configurations to examine the influence of the tip cap on the tip vortex formation and its subsequent roll-up process. These tip configurations are shown in cross section in Fig. 3 and consist of 1) a squared (or flat) tip-cap, 2) a rounded (or body of revolution) tip cap, and, 3) a beveled (or triangular) tip cap. The surface grids and the flowfield grids were generated using a parabolic solver of Edwards,[11] as mentioned earlier. An H-H grid topology was generated by this method for the three tip configurations, and Fig. 3 shows this H – H grid topology in the tip region for the square and triangular tip caps. The hyperbolic grid generator of Steger and Chaussee[14] was also used to construct spherically warped O-O grid topologies for the round tip and for a superellipse approximation to the square tip (ratio of major to minor axes = 15); this O-O grid is sketched in Fig. 3 for the round tip. It should be noted that solutions were computed for both H-H and O-O grid topologies. While the H-H grid was used with the TNS code, the O-O grid topology was used with the one-block flow solver of Ying et al.[15] This flow solver, called SF3D, is also a derivative of the ARC3D code[4] and has the same features of ARC3D code except that it uses upwinding in one of the coordinate directions and a partially flux-split algorithm. The flowfield computations were performed on the Cray-2 supercomputer with this code.

A representative surface grid for this wing (with beveled tip cap) is shown in Fig. 2a; it has 96 points (48 each on upper and lower surfaces) in the streamwise direction and 23 points along the span. This default grid has approximately 40,000 grid points in each of the four zones. The round and square tip-cap configurations, in contrast, have a much better surface definition in the tip region, with 57 points along the span but with the same number of streamwise points. This translates into about 90,000 grid points for each of the four zones. Typical computational times for the steady-state calculations, for a four-order drop in residuals with the TNS code, were of the order of 5–12 h on the Cray-XMP supercomputer, depending on the grid size. On the other hand, the single-block grids for these configurations (used with the SF3D code and Cray-2 supercomputer) had 155 points in the periodic (streamwise) direction, 66 in the spanwise direction, and 66 in the normal direction.

Typical results for this wing with different tip-cap options are shown in Figs. 4–7. Figure 4 shows the computed surface pressure distributions at several spanwise stations compared with the experimental data.[12,13] The results shown here for the inboard spanwise stations are essentially the same for all the tip-cap options and have a typical two-dimensional attached flow behavior, and these are in very good agreement with the experimental data. The leading-edge suction peak and local

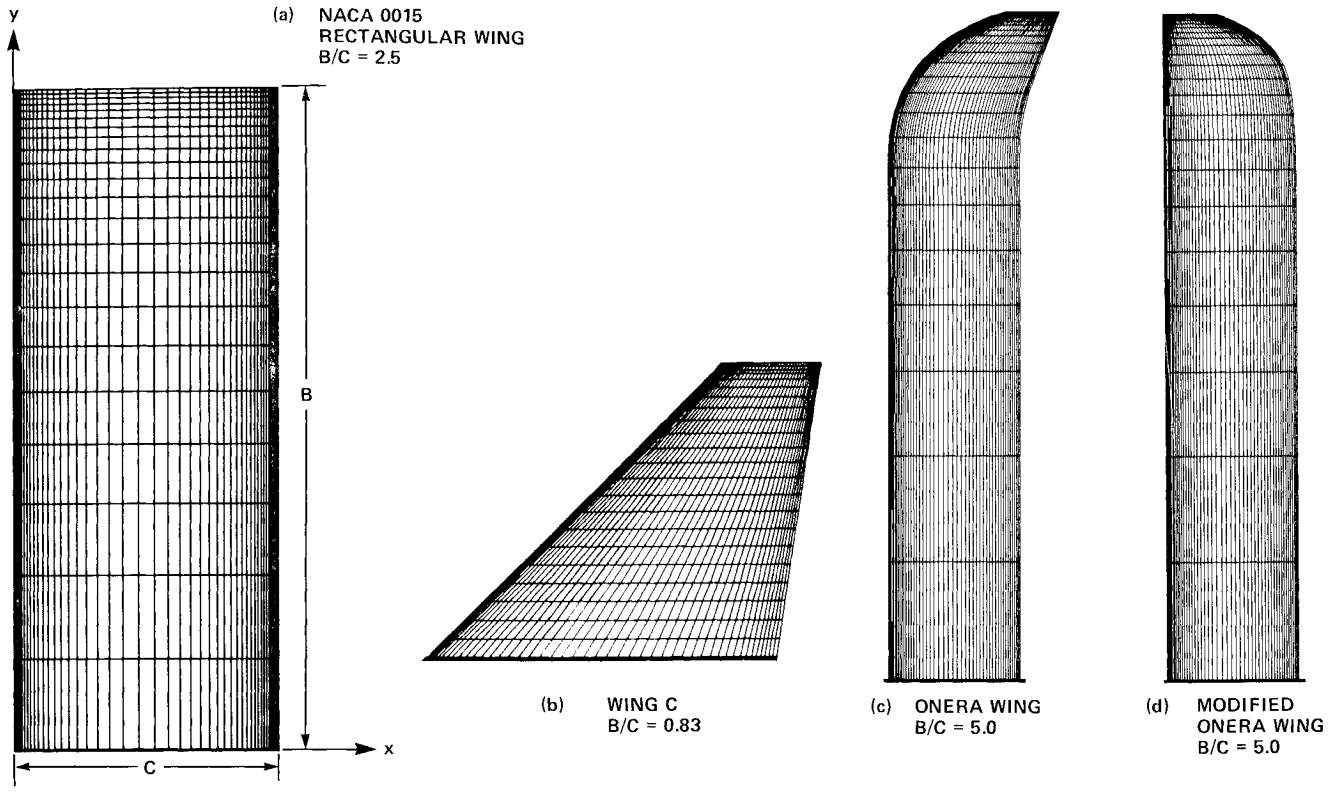

Fig. 2 Planforms and surface grids of the four test wings.

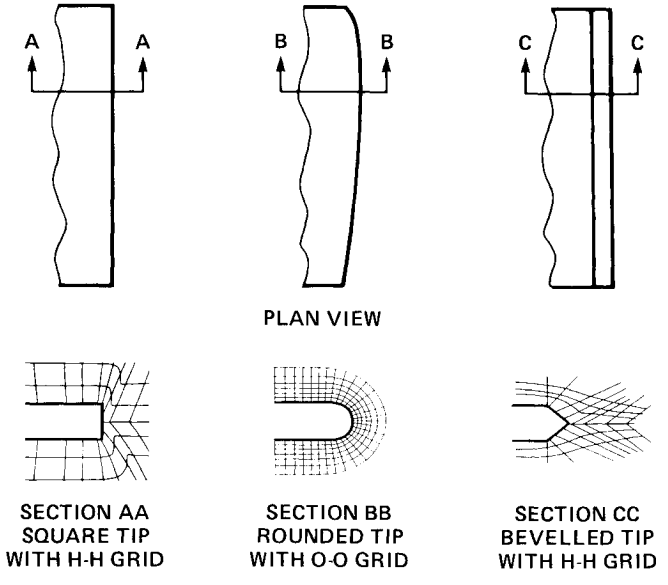

Fig. 3 Schematic of tip planforms and tip-cap shapes for NACA 0015 rectangular wing.

lift coefficient decrease monotonically from root to tip, as expected, due to the induced downwash of the tip vortex and wake vortex sheet. Although the three different tip caps produce very different flowfields in the tip region, the good agreement of the surface pressure distributions for about 90% of the span, as shown in Figs. 4a–4c, suggests that the influence of the tip-caps is restricted to the outer 5–10% of the span.

The flowfield in the tip region appears very different for each of these tip caps, as mentioned earlier. For example, the chordwise surface pressure data for the square tip wing of Refs. 12 and 13, shown in Fig. 5, show two suction peaks in

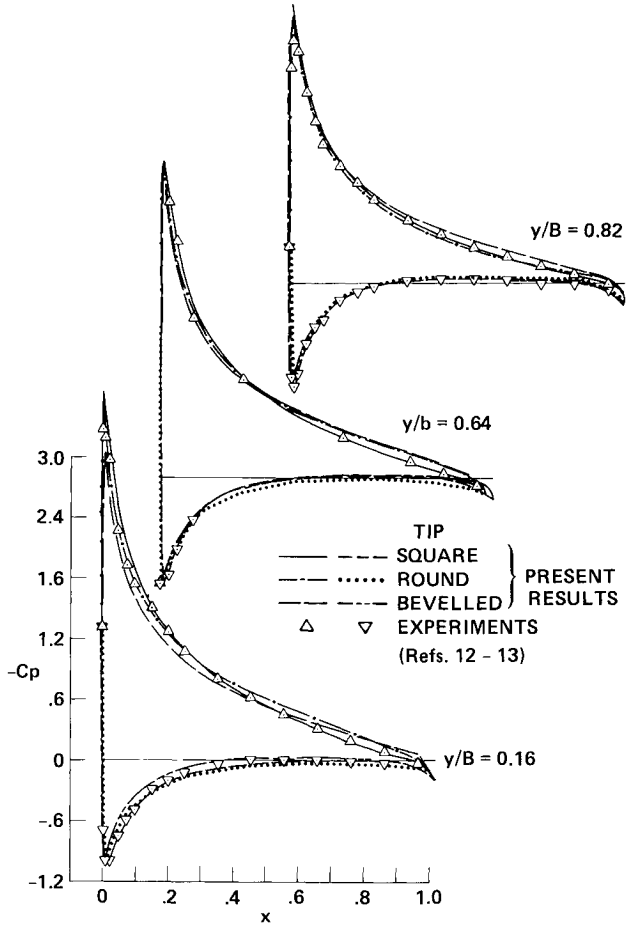

Fig. 4 Calculated surface pressure distributions for the rectangular wing with different tip caps compared with experimental data. $M_\infty = 0.17$, $\alpha = 11.8$ deg, and $Re = 2 \times 10^6$.

the tip region, besides the leading-edge suction peak. These are associated with the primary and secondary tip vortices created slightly inboard of the sharp edge on the upper surface of the wing; the primary peak occurs near the midchord, and the secondary peak is farther aft (toward the trailing edge) and more inboard. The presence of two peaks in the tip region has also been observed in the experiments of Triebstein[16] for the square-tip wing. The interaction of the primary vortex with the surface boundary layer is responsible for the creation of the counterrotating secondary vortex, which is similar to that observed on sharp-edged delta wings.[17]

The calculated surface pressure distributions in the tip region of the rectangular wing with different tip caps are compared to the experimental data of the square-tip wing.[12,13] As seen here for the square-tip configuration, the present calculations reproduce very well the evolution and disappearance of the suction peak due to the primary vortex, and the results are in good qualitative agreement with experiments. The location of the primary vortex is reasonably well predicted. The suction under both the primary and the secondary vortex, on the other hand, appears weaker compared to the experimental value and, in this part of the pressure distribution plots, the comparison is only qualitatively good, as noted earlier. Also, the separation bubble on the face of the tip, as visualized in the water-tunnel tests of Thompson,[18] was not resolved. No dramatic improvement was observed in these results when the grid resolution was increased by 50% in the tip region or even when the grid topology was changed from H-H to O-O type. Also, a laminar calculation for this case did not reproduce the suction peak due to the secondary vortex. The possible reasons for this could be the assumption of thin-layer equations, the use of a simple turbulence model, and inadequate grid resolution.

Figure 5 also shows the surface pressure distribution for the round-tip wing. In contrast to the observation of two suction peaks for the square tip-cap wing, the rounded tip cap produces only one suction peak, in agreement with the observation made by Triebstein.[16] The location of this suction peak is outboard and farther aft in comparison to the primary suction peak location of the square-tip wing. This implies that the vortex formation is delayed toward the trailing edge for the round-tip wing, unlike the wing with the square tip, for which the process seems to have started almost from the leading-edge region because of the larger extent of separated region. Also, because the extent of the suction peak is narrower in the spanwise direction, the vortex appears to be more tightly wound (smaller core size) than in the square-tip case.

In contrast, Fig. 5 shows no obvious suction peaks for the beveled tip-cap configuration. The flow in the tip region for the beveled-tip wing thus appears to be very different from that of the square-tip wing, although both these tip geometries have a tendency to separate the flow right at the leading edge. For the square-tip case, the flow going around the wing tip from the (high-pressure) lower surface to the (low-pressure) upper surface seems to delay the onset of separation to slightly downstream of the leading-edge region. For the beveled-tip wing, however, the separation point is fixed right at the sharp point of the leading edge of the tip. Further examination of this tip-cap geometry has revealed that its shape degenerates into a zero-thickness sharp point at the leading and trailing edges. The sharp corner at the wing-tip leading edge is responsible for producing a larger separated region than the square-tip wing would produce and thus masks the suction peak that would otherwise exist owing to the primary vortex. This observation is in good qualitative agreement with the water-tunnel flow visualization studies of Thompson.[18] As a consequence, the pressure field for this tip cap does not show any indication of the tip vortex presence from the surface pressure distributions. Otherwise, these results are in overall agreement with the results of other tip caps and of the experiment for the square tip at 97% span station as shown in Fig. 5 for the lower surface and up to about the midchord on the upper surface.

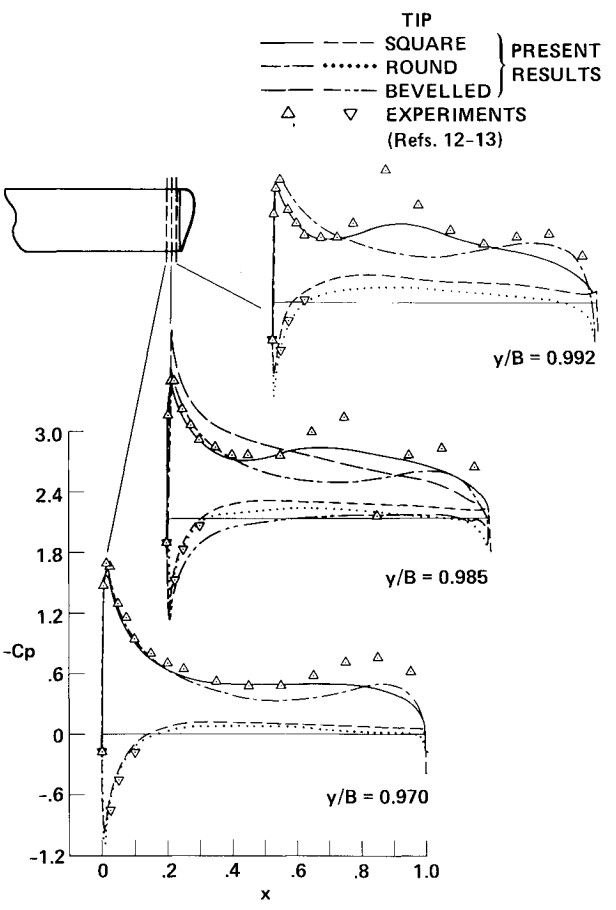

Fig. 5 Surface pressure distributions in the tip region for the rectangular wing with different tip caps. $M_\infty = 0.17$, $\alpha = 11.8$ deg, and $Re = 2 \times 10^6$.

Figure 6 shows the details of the surface "oil flow" pattern in the tip region for these three tip caps. (Computationally, the surface oil flow picture is generated by releasing fictitious fluid particle tracers at one grid point above the surface and restricting the paths of these particle tracers to lie in that plane.) An examination of these figures reveals that the square tip, Fig. 6c, produces the most complex separated flow pattern of the three tip caps considered here. The rounded tip cap, Fig. 6b, produces the least separation, and the beveled tip cap, Fig. 6d, produces the most. Comparison of the experimental surface oil flow for the rounded tip of Fig. 6a (reproduced from the ongoing experiments at the Army Aeroflight-dynamics Directorate at NASA Ames Research Center) with the computed flow of Fig. 6b shows excellent agreement in this region. The separation and reattachment lines observed in the experiment are well predicted. However, for the beveled tip-cap geometry, the extent of separation region on the wing is more pronounced than is apparent from the experimental pressure contour plot of Chigier and Corsiglia[19] for the square-tip wing, indicating that the beveled tip cap, first thought to mimic the experimental square tip, is really different and is neither a near-squared nor a near-rounded tip.

The close-up views of the formation and liftoff of the tip vortex for the round and square tips are shown in Fig. 7. These are constructed by releasing unrestricted fluid particle tracers at several locations along the chord and span and at different heights from the surface of the wing on both upper and lower surfaces. It is seen from this that the formation process of the tip vortex consists of the braiding of fluid particle tracers released from both upper and lower surfaces of the wing. The fluid particles released on the lower surface (high pressure side) smoothly cross over the wing tip and mix with the par-

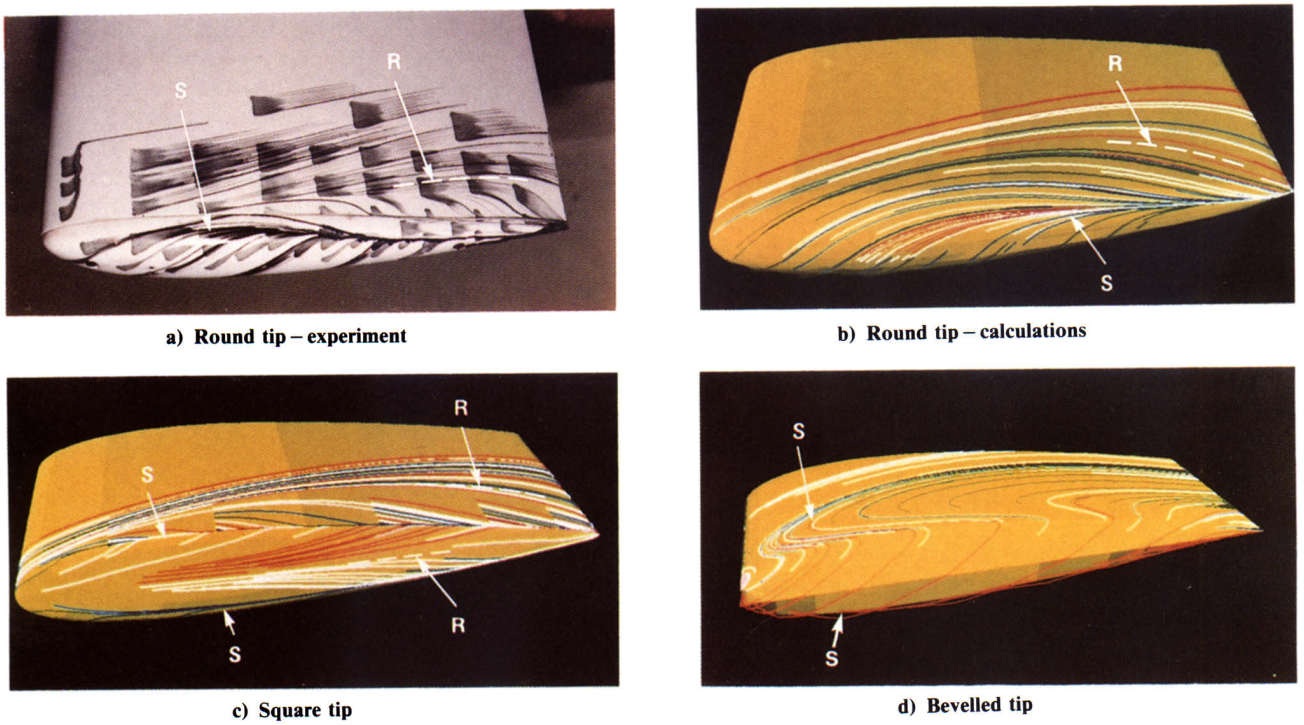

Fig. 6 Computed and experimental surface particle flow pattern in the tip region; $M_\infty = 0.17$, $\alpha = 11.8$ deg, and $Re = 2 \times 10^6$. The symbols S and R denote separation and reattachment lines.

ticles released on the upper surface and braid into each other. This tightly braided bunch of fluid particles defines a tip vortex that is distinct from the rest of the wake vortex sheet. While the braiding process is still in progress, the vortex lifts off the surface and, as it rolls up, it also starts rolling inboard of the wing tip. Further downstream of this, it continues to roll inboard and stays distinctly above the shed wake vortex sheet. The formation process of the tip vortex for both the round tip and the square tip wing begins well before the midchord position, as shown in Fig. 7. Because of the small extent of separation associated with the smooth curvature of the round tip cap, the liftoff of the vortex from the surface is delayed well into the trailing-edge region, as apparent from Fig. 7a. In contrast, the square tip cap, for which the extent of separation is larger, produces a tip vortex that lifts off from the surface around the midchord, as shown in Fig. 7b. It appears that the round tip produces a tightly braided tip vortex compared to the square tip. Also, the distinct separation of the tip vortex from the wake vortex sheet is clearly seen in these figures. For the square-tip wing, the primary and secondary vortices seem to merge into one distinct tip vortex in the downstream wake.

The lift, drag, and quarter-chord pitching-moment coefficients calculated for the square-tip wing are 0.762, 0.0886, and -0.004, respectively. This compares well with the measured data of 0.763, 0.0868, and -0.00843 for the lift, drag, and pitching-moment coefficients, respectively. (Tabulated data from experiments of Spivey and Moorhouse[12,13] were provided by U.S. Army Aeroflightdynamics Directorate.) From the lift coefficient, the approximate strength of tip vortex can be estimated using the definition of lift-equivalent vortex strength as 0.38. (Note that the vortex strength is nondimensionalized by the freestream velocity and the chord of the wing.)

Consistency of the vortical model was checked by comparing the value of $C_L/2$ with the line integral of the velocity vector q over a closed path s enclosing the tip vortex, that is,

$$\Gamma_V = \oint_s q \cdot ds \tag{4}$$

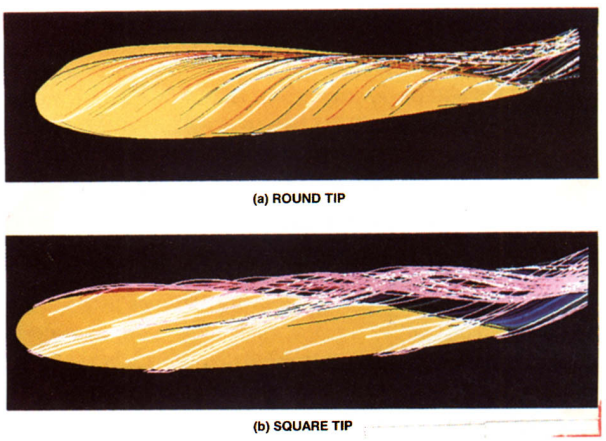

Fig. 7 Formation and liftoff of the tip vortex for the rectangular wing with: a) round tip; and b) square tip; $M_\infty = 0.17$, $\alpha = 11.8$ deg, and $Re = 2 \times 10^6$.

The result of such a line-integral over a path big enough to enclose the tip vortex at several x stations behind the wing gave a range of values from 0.37–0.41, depending on the size of the integration path around the vortex. The larger value corresponds to the case of the line-integral path extending all the way to the wing root in the y direction and extending to the limits of the grid in the z direction. The extent of this path is expected to include the contribution from the wake vortex sheet also.

Swept Tapered Wing in Transonic Flow

Transonic calculations were performed on an advanced technology wing, called wing C, which has been extensively studied both computationally[1,2] and in wind-tunnel experiments.[20,21] Its planform and the surface grid are shown in Fig. 2b. It is a low-aspect-ratio (equal to 0.83 based on the root chord) wing made up of supercritical wing sections, with a

twist angle of 8.17 deg, a taper ratio of 0.3, and a leading-edge sweep of 45 deg. As noted earlier, Mansour,[1] in a pioneering but limited study, attempted to simulate the flowfield in the tip region, including tip vortex formation for this wing in a freestream Mach number of 0.82 and at 5 deg angle of attack. Recently Kaynak et al.[2] have presented extensive computational results for this wing for a range of Mach numbers using the TNS code. Whereas the study of Ref. 2 concentrated on analyzing the flow topology, the present study focuses on the flow in the vicinity of the wing tip and, in particular, on the tip vortex phenomenon.

The freestream conditions for the present computations are $M_\infty = 0.9$, $\alpha = 5$ deg, and $Re = 6.8$ million, based on the mean aerodynamic chord. As before, the computational grid was generated first by a grid solver[11] with sufficient grid resolution in the wing-tip region to resolve the tip vortex. The interior grids were generated within the TNS code by the Zoner program. The CPU time for a fully converged solution was about 5 h for this case, which is highly transonic and has a shock-induced flow separation on the upper surface of the wing. Typical results of surface pressures are shown in Fig. 8 compared with the experimental data of Keener.[20] The agreement is very good over parts of the wing that do not have massive shock-induced separation, and the results are in general agreement with those of Ref. 2. With additional numerical experiments with the turbulence model and input from experiments for specifying the inflow and outflow boundary conditions, Kaynak and Flores[22] have recently demonstrated, with this code, that it is possible to model more accurately the shock-induced separation region also. However, such an exercise was not undertaken in the present investigation.

Tip vortex formation and subsequent roll-up was visualized as before by releasing fluid particle tracers at different locations along the chord and span and at various heights from the wing surface. Figure 9 shows some of the flow details for this wing, such as the λ-type shock wave and shock-induced separated flow, as well as a view of the tip vortex where the initial formation and subsequent roll-up process are clearly seen. As before, the tip vortex stays distinctly above the wake vortex sheet. Part of the separated flow from the shock-induced separated region lifts up from the wing surface and merges into the flow in tip region. The fluid particle tracers from this region get braided into the particle paths crossing over the tip from the high-pressure region of the wing lower surface, and together they separate out into the tip vortex and stay distinctly apart from the rest of the vortex sheet.

The view in Fig. 9 demonstrates clearly the way the vortex rolls inboard in the downstream wake after leaving the surface of the wing. The shape and strength of the tip vortex are apparent from the vorticity contours shown here at several x locations. These contours are shown as slices taken across the tip vortex in the y–z plane. In these the vorticity magnitude increases in the order of blue-yellow-red color. As the tip vortex is becoming diffused in the far-field coarse grid,[9] the magnitudes of the vorticity contours decrease and the cross section of the tip vortex appears to have stretched according to the grid-cell aspect ratio. But the line integral of the velocity vector around a closed path surrounding the tip vortex remains approximately constant as long as the integration path is large enough to contain the tip vortex. For this wing, the calculated values of the aerodynamic coefficients were $C_L = 0.361$, $C_D = 0.0347$, and $C_M = -0.146$. The strength of the vortex determined from the line-integral method yielded a value between 0.17 and 0.185, depending on the size of the integration path around the tip vortex. The larger value includes the vortex sheet in the wake and therefore corresponds to the larger path of the integral (usually extending to the symmetry plane in the y direction and to the boundaries in the z direction).

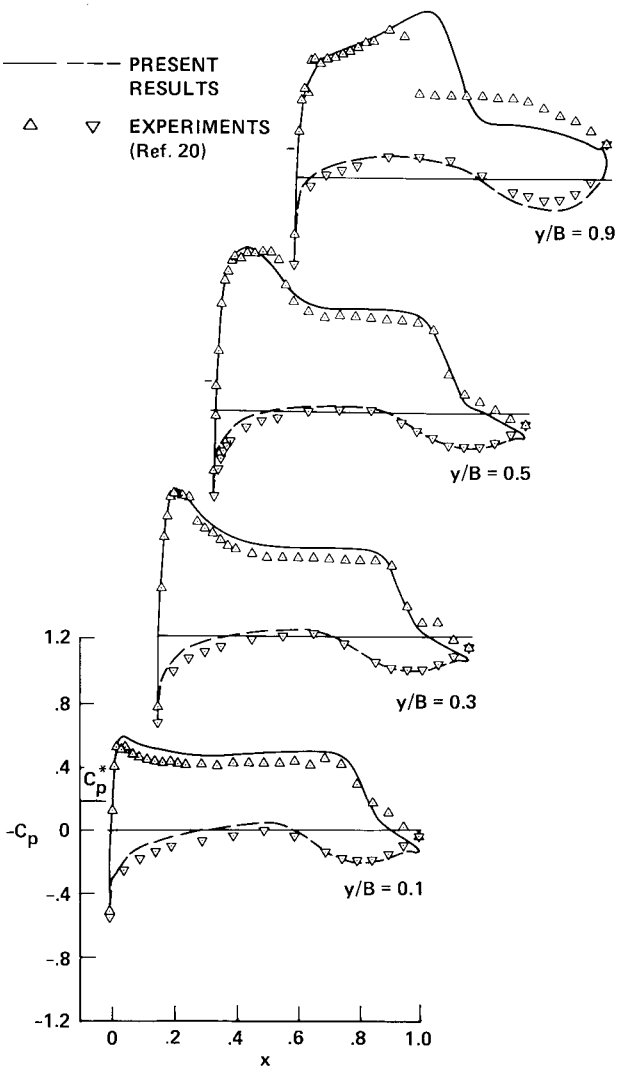

Fig. 8 Calculated and experimental surface pressure distributions for the swept tapered wing C; $M_\infty = 0.90$, $\alpha = 5$ deg, and $Re = 6.8 \times 10^6$.

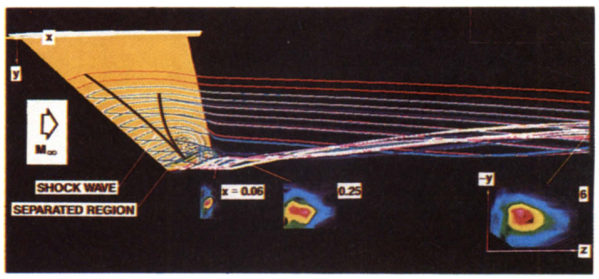

Fig. 9 Shock wave, separated region, vorticity contours, and far-field view of the tip vortex for wing C.

ONERA Wing in Transonic Flow

This wing has an aspect-ratio of 5 and represents a typical helicopter rotor blade.[23] The geometry for this wing has a combination of rectangular wing and swept-tip wing. The wing is made up of three special airfoil sections ranging in thickness from 12 to 6% from root to tip. The wing has a constant chord up to about 70% of the span station and tapers toward the tip. The surface grid for this wing has only 23 spanwise stations (for the default grid size) in the fine Euler and viscous zones and hence is very sparse in this direction, as shown in Fig. 2c. For this wing in a uniform freestream of $M_\infty = 0.85$, $\alpha = 5$ deg, and $Re = 8.5$ million (based on the root chord), computations were carried out to generate a steady-state solution.

Figure 10 shows the computed surface-pressure distributions for several spanwise stations along the wing. Examination of these indicates the presence of a strong shock wave on

the upper surface, which produces a complex large-scale separation. The leading-edge spikes seen in the pressure distributions are due to the poor leading-edge definition of the wing. This was verified independently by making two-dimensional calculations for several sections of the wingspan with refined leading-edge definition. The surface flow pattern for this configuration shows important topological features of a complex separated flow, and an outward spiraling vortex emanates from this separated region.[24]

Figures 11 and 12 show two views of the tip vortex for this wing. The initial formation process of the vortex and lifting off from the wing surface are shown in Fig. 11. The crossflow due to the swept-tip shape of the wing enables the fluid particles released in the vicinity of the tip to merge and braid into a distinct tip vortex. Also, the fluid particles released on the high-pressure side of the wing (lower surface) at the tip cross over the low-pressure side (upper side) by wrapping around the wing tip and braid into the swirling tip vortex. For this tip geometry, the intricate braiding of fluid particle tracers appears to produce a much tighter vortex than in any of the other cases considered. Figure 12 shows the far-field view of this tip vortex. The liftoff of the tip vortex from the wing surface and then the roll-up in the downstream wake and the inward migration are clearly evident in this photograph. Also shown here is the strong transonic shock wave and associated massive shock-induced separation and reattachment (shown as dashed line parallel to the trailing edge). In addition, the vorticity contours drawn in the y-z planes through the tip vortex at several x locations behind the wing suggest approximate vortex strengths and shapes at these locations. As observed before, the vorticity levels of the contours decrease in the downstream coarse-grid region of Block 1, and the shapes of these contours (and hence the shape of the tip vortex) become stretched in the pattern of the grid geometry.

The lift, drag, and the pitching-moment coefficients for this wing are respectively $C_L = 0.26$, $C_D = 0.061$, and $C_M = 0.002$. It should be pointed out here that this particular configuration is not designed to operate in a uniform freestream, but rather to operate as a helicopter blade for which the speed increases from the root to the tip in a linear fashion. Therefore, it is not surprising to note a slightly positive (destabilizing) pitching moment for this wing. Based on the definition of lift-equivalent vortex strength, the nondimensional tip vortex strength for this wing is 0.13. Also, the value of Γ_V determined from the line integral of the velocity vector around a closed path surrounding the vortex and at several x locations in the wake is in the range 0.12–0.14, depending on the path of the integral. The smaller value corresponds to the smaller integral path surrounding the tip vortex. The larger value includes the effect of wake vortex sheet.

Effect of Tip Planform

To study the influence of the tip planform geometry on the tip vortex formation, the ONERA wing of Fig. 2c was modified to reshape the planform in the tip region, keeping the rest of the geometry the same. The planform and the surface grid for this modified wing is shown in Fig. 2d. This modified wing geometry has an unswept leading edge and looks more like a rectangular wing, except that the tip region retains the original ONERA wing taper. The freestream flow conditions are identical to the preceding case. From the steady-state results for this wing, the lift, drag, and the pitching-moment coefficients for this wing are $C_L = 0.332$, $C_D = 0.0796$, and $C_M = -0.018$. The significant changes here are the larger force coefficients and the stabilizing pitching moment, in contrast to the slightly destabilizing value for the ONERA wing.

For this case, the shock wave and the resulting shock-induced separation are stronger than for the ONERA wing, and the flow topology is different. Another important difference is the structure of the tip vortex. Figure 13 shows a view of the tip vortex for this wing. The formation of a tip vortex, which involves braiding of fluid particle paths, is delayed toward the trailing edge and the near wake region as seen in Fig. 13; also, the vortex appears more diffuse with a larger core. The nondimensional tip vortex strength determined from integrating the velocity vector around a closed

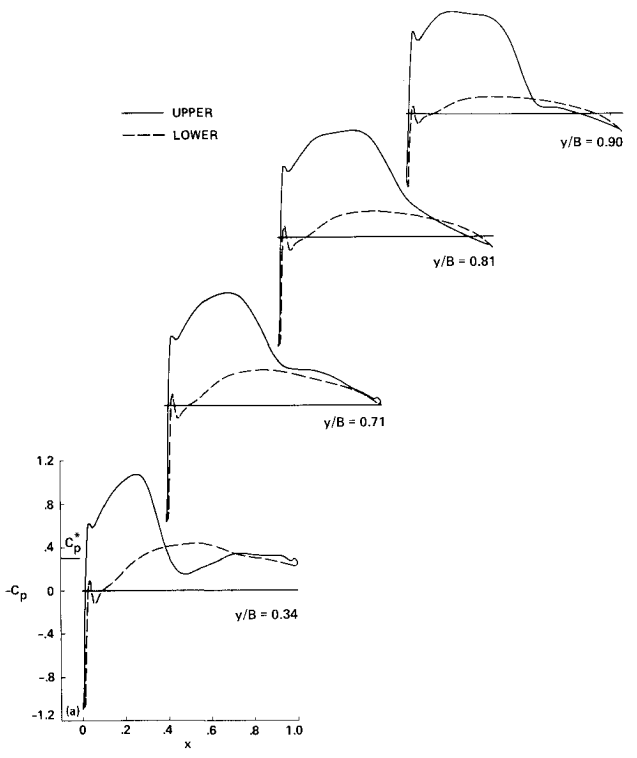

Fig. 10 Surface pressure distributions for the swept-tip ONERA wing. $M_\infty = 0.85$, $\alpha = 5$ deg, and $Re = 8.5 \times 10^6$.

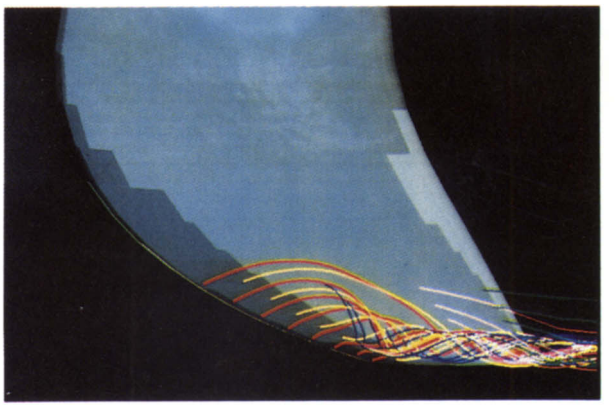

Fig. 11 Tip region of the ONERA wing.

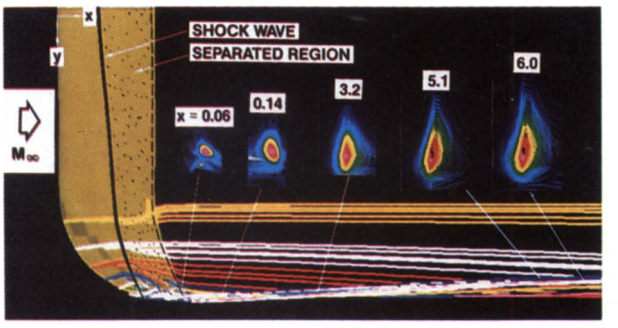

Fig. 12 Far-field view and vorticity contours of the ONERA wing.

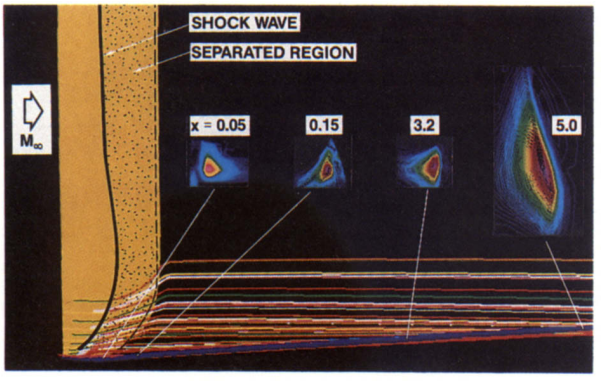

Fig. 13 Far-field view and vorticity contours for the modified ONERA wing. $M_\infty = 0.85$, $\alpha = 5$ deg., and $Re = 8.5 \times 10^6$.

path surrounding the tip vortex yields a value of 0.21 when the path of the integral includes the vortex sheet of the wake and a value of 0.17 for the path excluding most of the wake vortex sheet.

Conclusions

A multiblock zonal algorithm is used for solving the Euler and the Navier-Stokes equations to simulate numerically the formation and roll-up of tip vortices for wings in subsonic and transonic flows. In all, four different wing geometries have been used as test cases. The influence of the tip planform, tip-cap shape, and freestream Mach number on the formation process has been studied. The numerical results presented here required about 5-12 h of CPU time on the Cray-XMP supercomputer for each steady-state solution, depending on the grid size used.

Comparison of the numerical results with the limited available experimental data for both the subsonic and the transonic conditions showed good agreement for the surface pressures, except in the immediate vicinity of the tip and in the shock-induced separated region. The disagreement of surface pressures in the separated region is representative of the current state-of-the-art for predicting transonic shock-induced boundary-layer separation. The subsonic calculations reproduce the qualitative behavior of the experimental tip vortex formation, including the changes in the tip flow separation and in the vortex lift off due to rounded tip caps that have been observed experimentally. The use of a beveled tip cap to mimic a square tip was found to be an inadequate choice. The square-tip simulations do reproduce the correct locations of the suction peaks associated with primary and secondary vortices, but they fail to produce the correct magnitudes for the suction peaks under the vortex. Change of grid topology from H-H to O-O reproduced the same solution without any improvements. These errors may be due to the thin-layer assumption, to the deficiencies of a simple turbulence model, and possibly to inadequate grid resolution. Nevertheless, it has been demonstrated that it is possible to calculate the initial development of the tip vortex without ad hoc modeling. The limited study of the tip-cap effect on the flowfield near the tip region, presented here, suggests that the tip shape is an important ingredient of the problem.

As expected, the formation of the tip vortex involves braiding of the fluid particle paths in the tip region from both the upper and lower surfaces of the wing. For a lifting wing, the particles from underneath the wing (high-pressure side) cross over the tip face to the upper surface (low-pressure side) and modify the flowfield in the tip region by the three-dimensional tip-relief action. The tip vortex first lifts off the surface and then rolls up and moves inboard of the tip, staying distinctly above the wake vortex sheet. Both the tip-cap modification and the tip-planform change influenced the gross lift of the wing and hence of the tip vortex strength. The swept-tip planform had a weaker shock wave, but it also produced a more tightly wound (smaller core) vortex compared to the unswept tip.

In summary, the results presented here demonstrate that although there is still room for improvement, realistic and meaningful three-dimensional calculations of viscous flows over wings and their associated tip vortex formation are now feasible. This computational fluid dynamics capability provides a new tool for analyzing and improving the aerodynamic characteristics of wings and rotor blades.

Acknowledgments

The first author would like to acknowledge the support of this research by the U.S. Army Research Office under Contract DAAG29-85-C-0002, with Dr. Robert E. Singleton as the technical monitor. The computational time was furnished by the Applied Computational Fluids Branch of NASA Ames Research Center. The authors would like to express their sincere thanks to the members of TNS Group, and in particular to Drs. T. L. Holst and U. Kaynak, for several useful discussions. The graphics work presented here was generated using the PLOT3D graphics package developed by Dr. P. G. Buning of NASA Ames Research Center. ONERA wing coordinates were supplied by Drs. C. Tung and F. H. Schmitz of the U.S. Army Aeroflightdynamics Directorate at NASA Ames Research Center.

References

[1]Mansour, N.N., "Numerical Simulation of the Tip Vortex Off a Low-Aspect Ratio Wing at Transonic Speed," *AIAA Journal,* Vol. 23, Aug. 1985, pp. 1143-1149.

[2]Kaynak, U., Holst, T., Cantwell, B.J., and Sorenson, R.L., "Numerical Simulation of Transonic Separated Flows over Low-Aspect Ratio Wings," *Journal of Aircraft,* Vol. 24, Aug. 1987, pp. 531-539.

[3]Pulliam, T.H. and Steger, J.L., "Implicit Finite-Difference Simulations of Three-Dimensional Compressible Flow," *AIAA Journal,* Vol. 18, Feb. 1980, pp. 159-167.

[4]Pulliam, T.H., "Euler and Thin-Layer Navier-Stokes Codes: ARC2D, ARC3D," *Notes for the Computational Fluid Dynamics User's Workship,* Univ. of Tennessee Space Institute, Tullahoma, TN, March 1984.

[5]Holst, T.L., Gundy, K.L., Flores, J., Chaderjian, N.M., Kaynak, U., and Thomas, S.D., "Numerical Solution of Transonic Wing Flows Using an Euler/Navier-Stokes Zonal Approach," *Journal of Aircraft,* Vol. 24, Jan. 1987, pp. 17-24.

[6]Flores, J., "Convergence Acceleration for a Three-Dimensional Euler/Navier-Stokes Zonal Approach," *AIAA Journal,* Vol. 24, Sept. 1986, pp. 1441-1442.

[7]Beam, R. and Warming, R.F., "An Implicit Finite-Difference Algorithm for Hyperbolic Systems in Conservation Law Form," *Journal of Computational Physics,* Vol. 22, Sept. 1976, pp. 87-110.

[8]Pulliam, T.H. and Chaussee, D.S., "A Diagonal Form of an Implicit Approximate-Factorization Algorithm," *Journal of Computational Physics,* Vol. 39, Feb. 1981, pp. 347-363.

[9]Srinivasan, G.R., Chyu, W.J., and Steger, J.L., "Computation of Simple Three-Dimensional Wing-Vortex Interaction in Transonic Flow," AIAA Paper 81-1206, June 1981.

[10]Baldwin, B.S. and Lomax, H., "Thin Layer Approximation and Algebraic Model for Separated Turbulent Flows," AIAA Paper 78-257, Jan. 1978.

[11]Edwards, T.A., "Noniterative Three-Dimensional Grid Generation Using Parabolic Partial Differential Equations," AIAA Paper 85-0485, Jan. 1985.

[12]Spivey, W.A. and Moorhouse, G.G., "New Insights into the Design of Swept-Tip Rotor Blades," 26th Annual National Forum of the American Helicopter Society, Washington, DC, June 1970.

[13]Spivey, W.A., "A Study to Investigate the Aerodynamics of Rotor Blade Tip Shapes," Bell Helicopter Company Rept. 299-099-468, Jan. 1970.

[14]Steger, J.L. and Chaussee, D.S., "Generation of Body-Fitted Coordinates Using Hyperbolic Partial Differential Equations," *Journal of Scientific Statistical Computation,* Vol. 1, Dec. 1980, pp. 431-437.

[15]Ying, S.X., Steger, J.L., Schiff, L.B., and Baganoff, D., "Numerical Simulation of Unsteady, Viscous, High-Angle-of-Attack Flows Using a Partially Flux-Split Algorithm," AIAA Paper 86-2179, Aug. 1986.

[16]Triebstein, H., "Unsteady Pressure Measurements in Rotor Blade Tips with Incidence in Incompressible Flow," European Space Agency Technical Translation, ESA-TT-374, July 1977.

[17]Thomas, J.L., Taylor, S.L., and Anderson, W.K., "Navier-Stokes Computations of Vortical Flows Over Low Aspect Ratio Wings," AIAA Paper 87-0207, Jan. 1987.

[18]Thompson, D.H., "A Flow Visualization Study of Tip Vortex Formation," Aeronautical Research Laboratories, Melbourne, Australia, ARL-AERO-NOTE-421, Aerodynamics Note 421, Nov. 1983.

[19]Chigier, N.A. and Corsiglia, V.R., "Tip Vortices—Velocity Distributions," NASA TM X-62,087, Sept. 1971.

[20]Keener, E.R., "Computational-Experimental Pressure Distributions on a Transonic Low-Aspect-Ratio Wing," AIAA Paper 84-2092, Aug. 1984.

[21]Hinson, B.L. and Burdges, K.P., "Acquisition and Application of Transonic Wing and Far-Field Test Data for Three-Dimensional Computational Method Evaluation," AFOSR-TR-80-0422, 1980.

[22]Kaynak, U. and Flores, J., "Advances in the Computation of Transonic Separated Flows Over Finite Wings," AIAA Paper 87-1195, 1987.

[23]Desopper, A., "Study of the Unsteady Transonic Flow on Rotor Blades with Different Tip Shapes," *Vertica,* Vol. 9, No. 3, 1985, pp. 257-272.

[24]Srinivasan, G.R., McCroskey, W.J., Baeder, J.D., and Edwards, T.A., "Numerical Simulation of Tip Vortices of Wings in Subsonic and Transonic Flows," AIAA Paper 86-1095, May 1986.